ROYAL SOCIETY OPEN SCIENCE

royalsocietypublishing.org/journal/rsos

Research

Cite this article: Iso Y, Eri M, Hiroyoshi R, Kano K, Isobe T. 2022 Improving the thermal resistance of fluorescent $CsPb(Br,I)_3$ perovskite quantum dots by surface modification with perfluorodecanoic acid. *R. Soc. Open Sci.* **9**: 220475.
https://doi.org/10.1098/rsos.220475

Received: 26 April 2022
Accepted: 12 July 2022

Subject Category:
Chemistry

Subject Areas:
materials science/nanotechnology/inorganic chemistry

Keywords:
caesium lead halide perovskite quantum dot, phosphor, photoluminescence, thermal resistance, heat degradation, surface ligand modification

Authors for correspondence:
Yoshiki Iso
e-mail: iso@applc.keio.ac.jp
Tetsuhiko Isobe
e-mail: isobe@applc.keio.ac.jp

This article has been edited by the Royal Society of Chemistry, including the commissioning, peer review process and editorial aspects up to the point of acceptance.

Electronic supplementary material is available online at https://doi.org/10.6084/m9.figshare.c.6135601.

ROYAL SOCIETY OF CHEMISTRY

THE ROYAL SOCIETY PUBLISHING

Improving the thermal resistance of fluorescent $CsPb(Br,I)_3$ perovskite quantum dots by surface modification with perfluorodecanoic acid

Yoshiki Iso, Momoko Eri, Risako Hiroyoshi, Kensho Kano and Tetsuhiko Isobe

Department of Applied Chemistry, Faculty of Science and Technology, Keio University, 3-14-1 Hiyoshi, Kohoku-ku, Yokohama 223-8522, Japan

YI, 0000-0001-7483-2828; TI, 0000-0002-0868-5425

$CsPb(Br,I)_3$ quantum dots (QDs) show application potential for optoelectronic devices. However, their thermal degradation is a significant problem. In this work, the effects of perfluorodecanoic acid (PFDA) modification on the photoluminescence (PL) and thermal resistance of $CsPb(Br,I)_3$ QDs were evaluated. The PL intensity of oleic-acid-modified quantum dots (OA-QDs) in toluene decreased drastically upon heating at 100°C. The PL quantum yield of the QDs increased from 69.6% to 77.4% upon modification with PFDA. Furthermore, the PL intensity of the QDs modified with PFDA (PFDA-QDs) increased to 140.6% upon heating, because of the reduction of surface defects upon adsorption of PFDA and its optimized adsorption state. A solid-film PFDA-QDs sample heated at 80°C for 4 h showed temporary PL enhancements for the OA-QDs and PFDA-QDs films to 445% and 557% of their initial values, respectively, upon heating for 0.25 h. This was attributed to the optimized adsorption states of the surface ligands. PFDA-QDs film maintained 354% after 4 h of heating, whereas that of OA-QDs film was 104%. Thus, PFDA modification enhances PL intensity and suppresses PL degradation under heating, which is important for wavelength converters for optoelectronic device applications.

1. Introduction

$CsPbX_3$ (X = Cl, Br, I) perovskite quantum dots (QDs) have attracted extensive research attention owing to their excellent properties, including their bandgap (E_g) tunability (by halide composition), narrow luminescence peaks and high photoluminescence (PL) quantum yields (PLQYs) [1,2]. Accordingly, $CsPbX_3$ QDs have been applied in LEDs [3–10], wide-gamut displays [11–14], lasers [15–17], scintillators [18] and photovoltaic devices [19–24]. However, like organic–inorganic perovskite QDs, all-inorganic $CsPbX_3$ QDs are insufficiently durable for practical use yet. Thus, the development of strategies for improving their resistance to degradation by heat, excitation light, ambient air and/or moisture are required. Accordingly, numerous reports on improving the stability of $CsPbX_3$ QDs by various techniques [25], including B-site doping (for ABX_3 perovskites) [26,27], surface-defect elimination [28,29], the use of core–shell architectures [30] and matrix encapsulation [31], have been reported.

The current authors have focused on the effects of surface ligands on fluorescent QDs. Surface ligands protect QDs from surrounding molecules, passivate surface defects that cause non-radiative relaxation and provide dispersibility in solvents. Therefore, the state of adsorbed surface ligands is an important factor for the quality of fluorescent QDs. Oleic acid (OA) is generally used as a surface ligand in the traditional preparation of $CsPbX_3$ QDs. However, its desorption from the QDs causes significant degradation of their PL properties [32,33]. The acid dissociation constant (pK_a) of an alkylcarboxylic acid indicates its frequency of deprotonation and thus its adsorptivity as a surface ligand, because carboxylic acids coordinate to crystal surfaces in the deprotonated state. Fluorocarboxylic acids, which have electron-withdrawing fluorine atoms, exhibit lower pK_a values than OA [34]. The pK_a values of perfluorodecanoic acid (PFDA) and OA are 2.58 and 6.2, respectively [35,36]. Thus, the deprotonated state of PFDA is more stable than that of OA, so it should more readily adsorb onto a QD surface.

Monohalide $CsPbX_3$ QDs are not suitable for certain optoelectronic device applications. Instead, desired PL properties are realized by precisely tuning the composition of mixed-halide QDs. I-doped $CsPbBr_3$ QDs (typically represented by the label $CsPb(Br,I)_3$ QDs) realize green emission, the colour of which is very close to the vertex of chromaticity coordinate in the Rec.2020 standard for wide-colour-gamut displays [13,37]. However, mixed-halide QDs can be subject to partial decomposition and/or dissolution, changing the halide compositional ratio and thus leading to shifts in their absorption and emission wavelengths.

In this work, PFDA modification of OA-adsorbed $CsPb(Br,I)_3$ QDs was performed to investigate its effect on thermal resistance. Toluene dispersions of the as-prepared QDs and PFDA-modified QDs were heated at 100°C. Decanoic acid (DA) modification was also performed as a control procedure. Furthermore, solid films of the QDs obtained by vacuum drying were also evaluated.

2. Experimental

2.1. Materials

Cs_2CO_3 (99.99%) was purchased from Mitsuwa Pure Chemical. PbO (99.9%), toluene (>99.5%), acetone (>99.5%) and methyl acetate (>99.5%) were purchased from Kanto Chemical. OA (>85.0%), tetra-*n*-octylammonium bromide (>98.0%), tetra-*n*-octylammonium iodide (>98.0%) and DA (>98.0%) were purchased from Tokyo Chemical Industry. PFDA (98%) was purchased from Sigma-Aldrich. Toluene, acetone and OA were dehydrated over molecular sieves (3Å 1/8, FUJIFILM Wako Pure Chemical) prior to use.

2.2. Synthesis of $CsPb(Br,I)_3$ QDs and surface modification

The synthesis of $CsPb(Br,I)_3$ QDs by the ligand-assisted reprecipitation (LARP) method expanded upon those detailed previously [34]. Cs_2CO_3 (163 mg), PbO (223 mg) and 5 ml of OA were mixed and heated at 160°C to obtain a clear solution, which was then dehydrated for 30 min at 120°C. After cooling and adding 5 ml of toluene, 1 ml of this solution was added to a glass vessel containing 15 ml of toluene under vigorous stirring at room temperature. A clear halide solution was prepared by heating a mixture of tetra-*n*-octylammonium bromide (38 mg), tetra-*n*-octylammonium iodide (18 mg), 5 ml of OA and 2 ml of toluene at approximately 50°C. Here, the nominal ratio of Br : I was 70 : 30. The halide solution was swiftly added to the glass vessel at room temperature to synthesize $CsPb(Br,I)_3$ QDs.

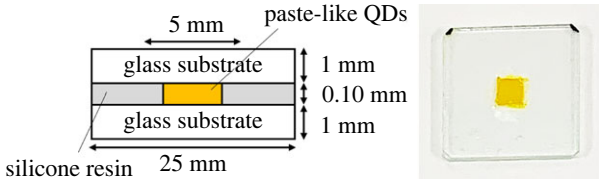

Figure 1. Schematic and photograph of a QD-film sample.

After 10 s, the QDs were precipitated by adding 50 ml of acetone and then collected by centrifugation at approximately 19 000×*g* (13 000 r.p.m. using a rotor of 10 cm in radius) for 5 min. The collected QDs were redispersed in toluene under ultrasonication and stirring to prepare an OA-QDs dispersion. The concentration was adjusted with reference to absorbance as described in a later section.

DA-QDs and PFDA-QDs dispersions were prepared by adding DA and PFDA, respectively, to the OA-QDs dispersion to achieve a concentration of 0.06 mmol l^{-1}. The prepared QD dispersions were sealed and stored under ambient conditions in the dark. To evaluate their thermal stabilities, the QD dispersions were heated at 100°C for 4 h in an incubator (HB-100, Taitec) with shaking at 60 r.p.m., and then cooled to room temperature before analysis.

2.3. Preparation of solid-film samples

Film samples were prepared to evaluate the properties of solid QDs. 15 ml of toluene was mixed with 1 ml of metal-ion solution and halide solution to nucleate $CsPb(Br,I)_3$ QDs. After 10 s, 200 µl of a toluene solution of PFDA at 10.8 mg l^{-1} was added to the obtained QD dispersion and aged for 1 min. PFDA-modified QDs were precipitated by adding 50 ml of methyl acetate and collected by centrifugation at approximately 19 000×*g* (13 000 r.p.m. using a rotor of 10 cm in radius) for 5 min. The precipitation was dried under vacuum for 12 h to obtain a paste-like solid sample of the PFDA-QDs. Paste-like OA-QDs were also prepared in the same way without adding PFDA. QD-film samples were prepared from the paste-like materials using glass substrates and silicone spacers, as shown in figure 1. To evaluate thermal stability, the film samples were heated at 80°C and 45% relative humidity for 4 h in a thermo-hygrostat (IG401, Yamato Scientific). It should be noted that the temperature used was the upper limit of the apparatus.

2.4. Characterization

X-ray diffraction (XRD) profiles were measured on an X-ray diffractometer (Rint-2200, Rigaku) using monochromatic CuKα radiation. Elemental compositions were determined using a wavelength dispersive X-ray fluorescence (XRF) analyser (ZSXmini II, Rigaku). Herein, wavelength dispersive mode was chosen to obtain reliable elemental compositions. For the XRD and wavelength dispersive XRF measurements, the centrifuged QDs were vacuum dried overnight. Fourier transform infrared (FT-IR) absorption spectra of QDs in pressed KBr discs were measured using a spectrometer (FT/IR-4200, JASCO). The particle images were captured with a field-emission transmission electron microscope (TEM; Tecnai G^2, FEI). Samples for TEM were prepared by drying a drop of the QD dispersion on a carbon-reinforced collodion-coated copper grid (COL-C10, Oken Shoji) overnight. Energy dispersive XRF analysis attached to the TEM was performed. Particle size distributions were determined by measuring 100 particles in TEM images at random. Evaluation of optical properties of the heated samples was performed after cooling to room temperature. Thermal analysis of the film samples was performed on a thermogravimetry analysis (TGA) instrument (Thermo Plus TG8120, Rigaku) in an Ar flow of 500 ml min^{-1} at a heating rate of 10°C min^{-1}. The UV–visible absorption spectra of the dispersions were measured using a UV/visible absorption spectrometer (V-750, JASCO). To ensure analysis at the same concentration, the net absorbance of the dispersion before heating was adjusted to 0.35 at 400 nm. The shown absorbance data are the net values calculated by subtracting the blank data for the pure solvent from the sample data. Tauc plots were prepared to determine the E_g values of the QDs according to equation (2.1) [38]:

$$(\alpha h\nu)^{1/n} = A(h\nu - E_g), \tag{2.1}$$

where α is the absorbance, h is the Planck constant, ν is the frequency and A is a constant. The value of n was 0.5 because cubic $CsPbX_3$ are direct-transition-type semiconductors [39]. The PL spectra were recorded on a

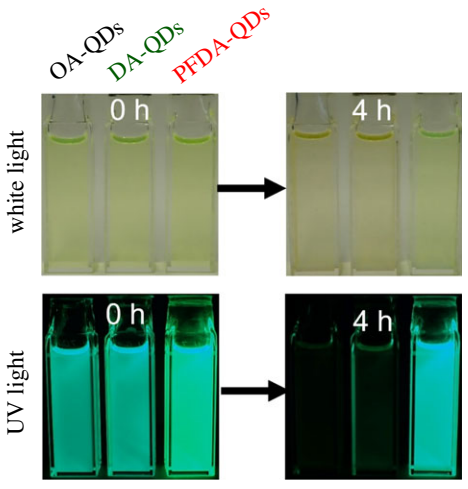

Figure 2. Photographs of QD dispersions under white light and 365 nm UV light before and after heating at 100°C for 4 h.

fluorescence spectrometer (FP-6500, JASCO). Herein, an ethylene glycol solution of rhodamine B (5.5 g l^{-1}) and a standard light source (ESC-333, JASCO) were used for calibration of each spectral response. Absolute PLQY values were determined using a quantum efficiency measurement system (QE-2000-311C, Otsuka Electronics).

3. Results and discussion

3.1. Effects of surface modification by PFDA on the thermal stability of $CsPb(Br,I)_3$ QD dispersions

Judging from the XRD profile (electronic supplementary material, figure S1), the as-prepared $CsPb(Br,I)_3$ QDs have a cubic crystal structure. The peaks in the XRD profile are between those corresponding to cubic $CsPbBr_3$ and cubic $CsPbI_3$. The Br : I ratio from wavelength dispersive XRF is 32.2 : 68.8, which is close to the nominal ratio of 30 : 70. Judging from the FT-IR spectra for the solid-film samples, PFDA-QDs contain PFDA with remaining OA (see electronic supplementary material, figure S2).

Figure 2 shows photographs of the QD dispersions before and after heating at 100°C for 4 h. The as-prepared PFDA-QDs dispersion shows brighter luminescence compared with the other dispersions. The PL peak for the PFDA-QDs dispersion is observed at 515.0 nm, which is a longer wavelength than those of the OA-QDs and DA-QDs dispersions (504.2 and 504.1 nm; electronic supplementary material, figure S3). Although the mechanism of the PL redshift is unclear, the adsorbed PFDA ligands might have a greater influence on the band structure of the QDs than the OA and DA ligands. Furthermore, PFDA modification enhances the PLQY from that of the OA-QDs dispersion (69.6%) to 77.4%, while DA addition results in no improvement. These results indicate that the strongly and frequently adsorbed PFDA ligands decrease the amount of surface defects on the $CsPb(Br,I)_3$ QDs.

After heating at 100°C for 4 h, a yellow precipitation of aggregated QDs is observed under white light for the OA-QDs and DA-QDs, while the PFDA-QDs show no change visible to the naked eye. Furthermore, extinction of the green emission under UV light occurs for the OA-QDs and DA-QDs, while the PFDA-QDs maintain their strong luminescence, even upon heating. These results indicate that surface modification with PFDA stabilizes the dispersibility and PL of the QDs.

Figure 3 shows TEM images of the QDs before and after heating at 100°C for 4 h (see also high-resolution TEM images in electronic supplementary material, figure S4). Particle size distributions were measured to determine the mean sizes of QDs (see electronic supplementary material, figure S5). The mean sizes of the OA-QDs, DA-QDs and PFDA-QDs are 9.2 ± 1.3, 8.9 ± 0.9 and 9.0 ± 1.1 nm; therefore, significant change was not observed by DA and PFDA additions. The mean size of the OA-QDs increases to 10.7 ± 1.5 nm during heating because of the dissolution and precipitation process. Crystal growth was also observed for the DA-QDs. However, PFDA modification maintains the size at 9.2 ± 1.4 nm, even after heating. Thus, the rigid surface adsorption of PFDA suppresses the dissolution

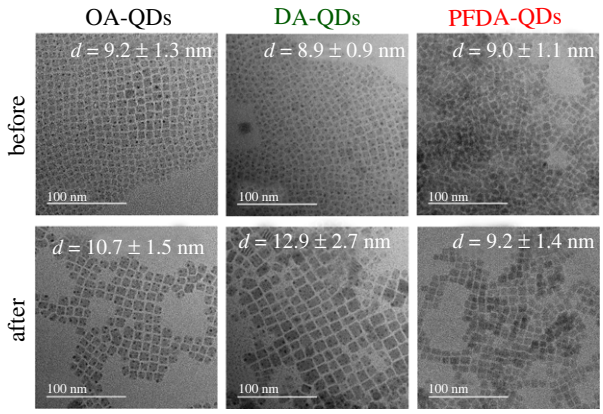

Figure 3. Particle morphologies observed by TEM for OA-QDs, DA-QDs and PFDA-QDs before and after heating at 100°C for 4 h.

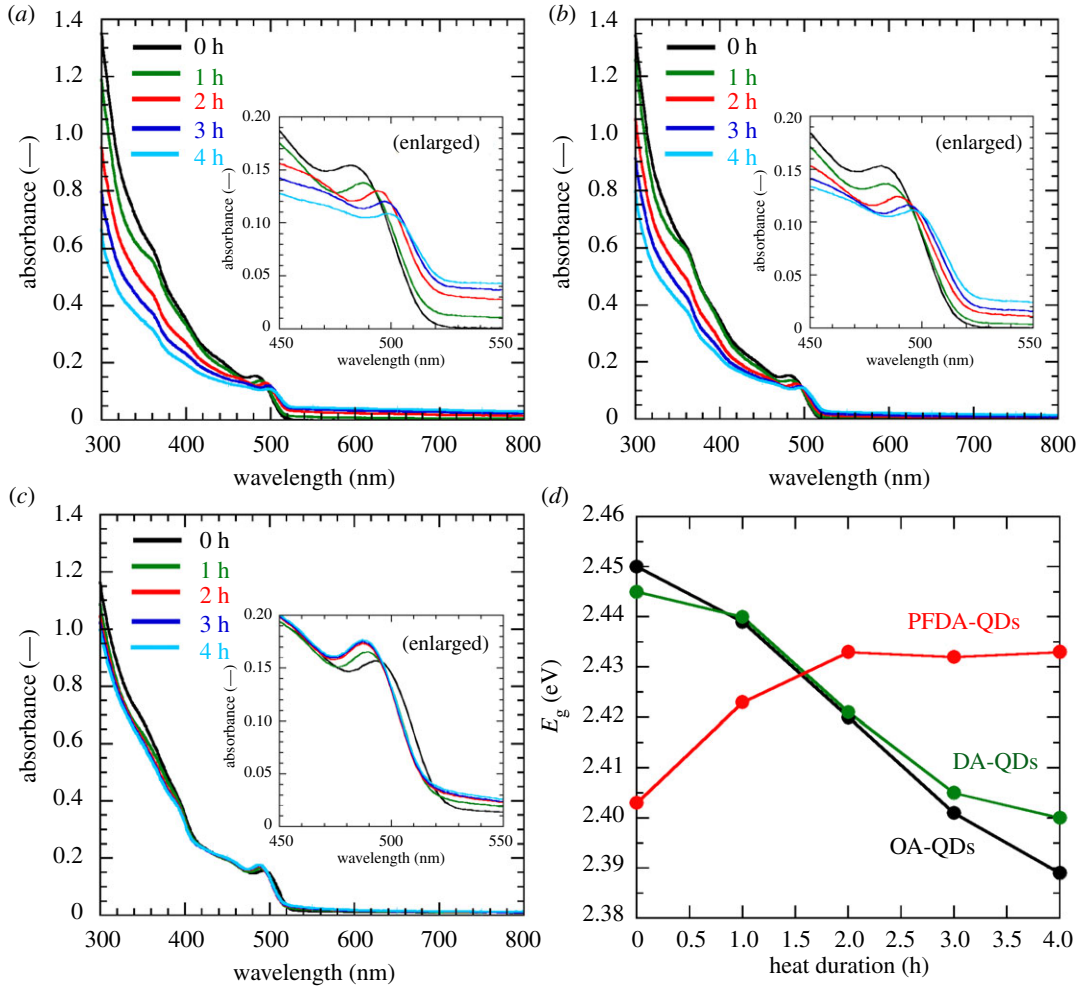

Figure 4. Changes in (*a–c*) UV–visible absorption spectra and (*d*) estimated E_g for the QD dispersions upon heating at 100°C. (*a*) OA-QDs, (*b*) DA-QDs and (*c*) PFDA-QDs.

and precipitation process. Furthermore, this also accounts for the excellent dispersibility of QDs upon heating (figure 2), because steric hindrance by the strongly adsorbed PFDA ligands prevents QD aggregation.

Figure 4*a–c* shows time-evolution UV–visible absorption spectra upon heating. The change in the spectra for the PFDA-QDs dispersions is smaller than those for the OA-QDs and DA-QDs dispersions. Heating the OA-QDs and DA-QDs dispersions for 4 h causes a slight redshift of the absorption edge

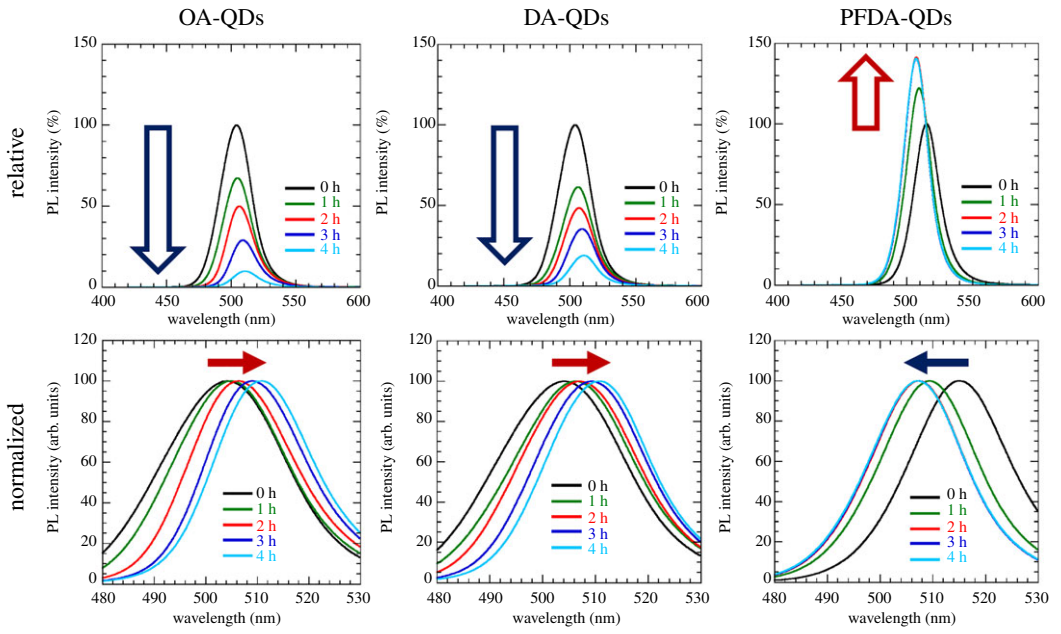

Figure 5. Changes in relative and normalized PL spectra for toluene dispersions of OA-QDs, DA-QDs and PFDA-QDs heated at 100°C. $\lambda_{ex} = 400.0$ nm.

and an increase in the baseline absorbance in the 500–800 nm range. This may be explained by increased light scattering due to the growth and aggregation of QDs and corresponds to the appearance of yellow aggregates in the OA-QDs and DA-QDs dispersions under white light.

E_g values were determined from Tauc plots of the UV–visible absorption data (see electronic supplementary material, figures S6–S8). Figure 4*d* shows the changes in the estimated E_g values. OA-QDs and DA-QDs dispersions show decreases in E_g upon heating. This is due to the quantum size effect that accompanies QD growth. By contrast, the PFDA-QDs dispersion shows an increase in E_g upon heating. This cannot be explained by the quantum size effect because no change in crystal size is observed in the TEM images. The E_g value of $CsPb(Br,I)_3$ QDs also varies with halide composition. The increase in E_g may result from the decrease in I/Br ratio, which occurs because of the preferential dissolution of iodine ions. Regrettably, precise elemental analysis by wavelength dispersive XRF was impossible because the PFDA-QDs could not be collected from the dispersion even after heating. Moreover, a reliable elemental composition was not determined by the energy dispersive XRF analysis attached to the TEM because of peak overlaps (see electronic supplementary material, figure S9).

Figure 5 shows the PL spectra of the dispersions measured at a room temperature. Here, the initial PL intensities were normalized to 100%. Changes in PL intensity and peak position with time are shown in figure 6. OA-QDs and DA-QDs dispersions show monotonic decreases in PL intensity to 9.8% and 18.8% upon heating, whereas the PFDA-QDs dispersion presents the highest PL intensity and no quenching throughout the experiment. Interestingly, the PL intensity increases until 2 h of heating, reaching 140.6%, indicating that a reduction in the number of surface defects, which cause non-radiative relaxation, occurs because of rapid adsorption of PFDA and its optimized adsorption state. Furthermore, the heat-ageing of QDs synthesized at room temperature by the LARP method might contribute to the improved PL intensity. The PL peak position for the OA-QDs dispersion shifts from 504.2 to 510.9 nm, while that for the DA-QDs dispersion also shows a redshift (from 504.1 to 510.8 nm). Conversely, a blueshift from 515.0 to 507.1 nm is observed for the PFDA-QDs dispersion. These shifts correspond to the changes in the absorption edges observed in figure 4. Therefore, the PL peak shifts can be explained by the same mechanisms used to rationalize the changes in E_g.

3.2. Effects of surface modification by PFDA on the thermal stability of $CsPb(Br,I)_3$ QD films

Figure 7 shows photographs of OA-QDs and PFDA-QDs films captured under white light during heating at 80°C for 4 h. The sample colour for both films under white light changes from yellow to orange. The photographs captured under 365 nm UV light show no specific change trend in PL intensity under UV

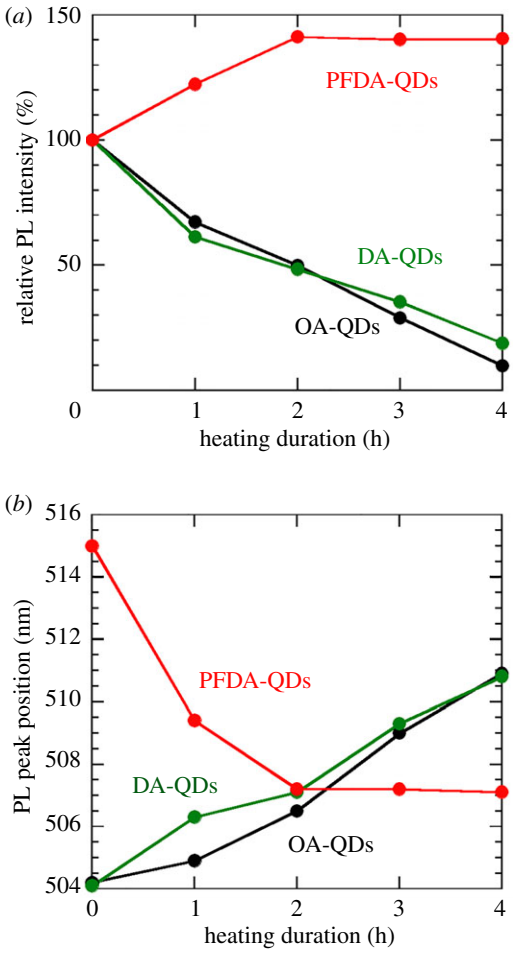

Figure 6. Changes in (*a*) PL peak intensity and (*b*) position (from data shown in figure 5).

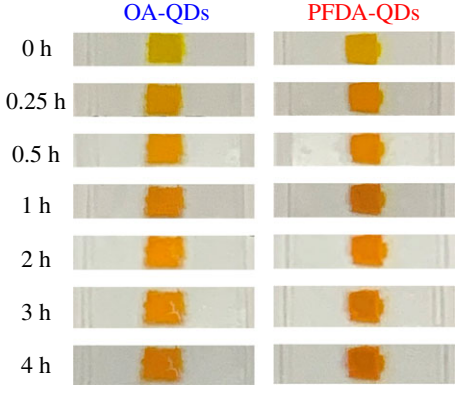

Figure 7. Photographs of QD films before and after heating at 80°C.

irradiation because of the automatic image adjustment of the digital camera (see electronic supplementary material, figure S10). Accordingly, reliable PL intensities were measured using a fluorescence spectrometer, as shown later. It should be noted that no significant PL quenching was observed by the naked eye.

TEM images of the film samples are shown in figure 8. Average particle size values were estimated from the size distributions (see electronic supplementary material, figure S11). The OA-QDs film shows a 38% increase in average size (from 6.5 ± 1.0 to 9.0 ± 1.3 nm) upon heating for 4 h. The film samples comprise paste-like QDs where many organic molecules surround the inorganic QDs. Thus, the crystal growth observed here may be caused by dissolution and reprecipitation through ion transfer

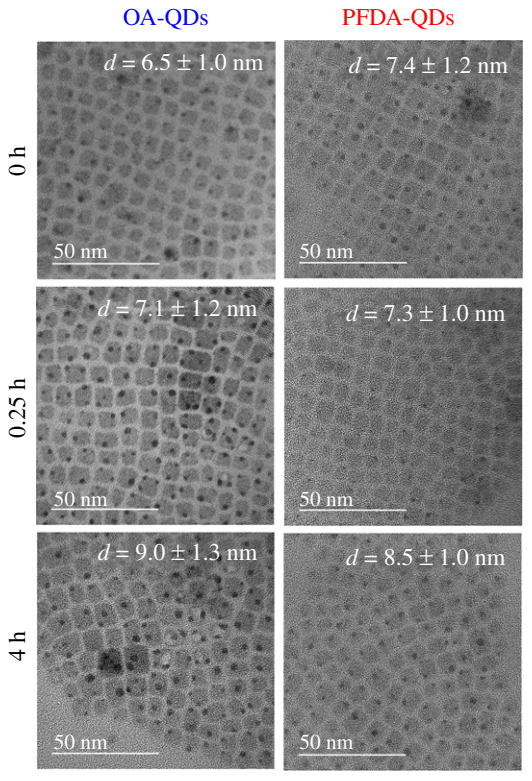

Figure 8. Particle morphologies of OA-QDs and PFDA-QDs films observed by TEM before and after heating at 80°C.

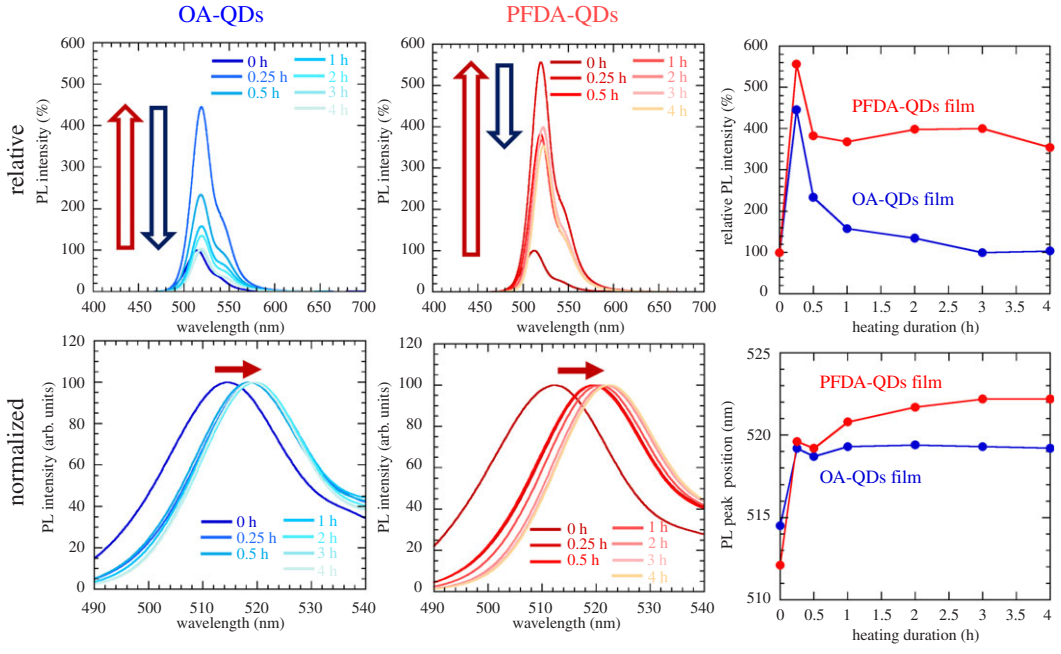

Figure 9. Changes in the relative and normalized PL spectra of QD films during heating at 80°C. The corresponding changes in PL peak intensity and position are also plotted.

among the organic molecules. Conversely, the PFDA-QDs film shows a 15% increase (from 7.4 ± 1.2 to 8.5 ± 1.0 nm) upon heating for 4 h. The rigid surface modification of PFDA prevents dissolution of the QDs, resulting in suppressed crystal growth during heating. TGA also exhibited improved thermal stability of PFDA-QDs (see electronic supplementary material, figure S12).

Figure 9 shows the PL spectra of the films measured at a room temperature. The time evolution of peak intensity and the peak shift are also summarized. The initial PL intensities before heating are

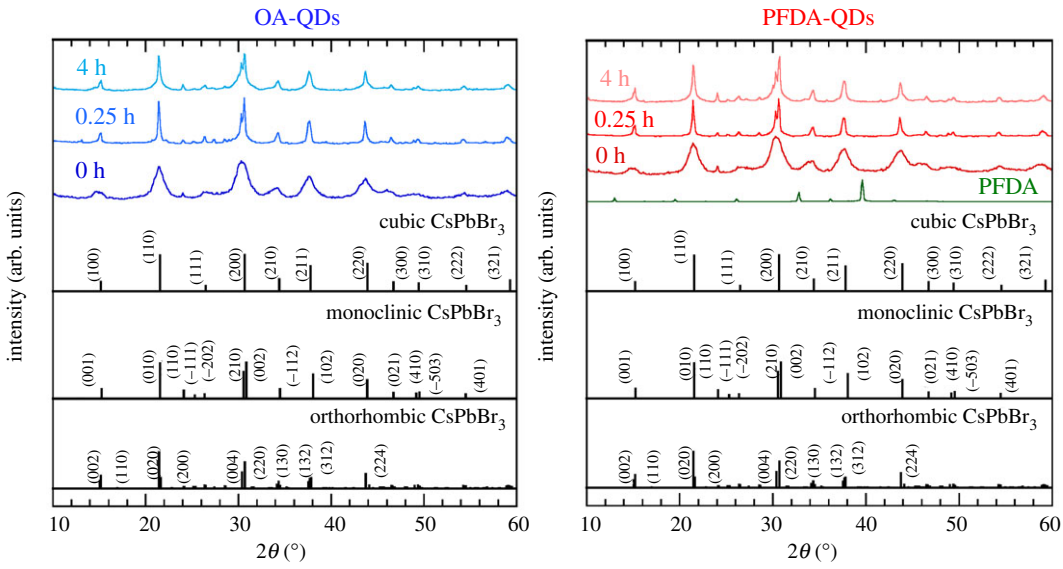

Figure 10. Changes in the XRD profiles of QD films during heating at 80°C. ICDD card data for cubic, monoclinic and orthorhombic $CsPbBr_3$ (nos. 00-054-0752, 00-054-0751 and 01-072-7929) are also shown.

normalized to 100%. A shoulder peak at longer wavelength is observed for the dried film samples, as reported in our previous works [32,33,40]. This may be explained by the photon recycling effect [41]. The PL intensities for the OA-QDs and PFDA-QDs increase to 445% and 557%, respectively, upon heating for 0.25 h, but they both decrease upon further heating. This PL increase may be attributed to the optimized adsorption states of ligands and improved crystallinity upon heat-ageing. Judging from the XRD profiles in figure 10, the cubic phase of $CsPb(Br,I)_3$ is converted to monoclinic or orthorhombic phases. Regrettably, the monoclinic and orthorhombic phases could not be accurately distinguished because their patterns are very similar. However, they are emissive and non-emissive phases, respectively. The decrease in PL intensity may be caused by a partial phase transition to the non-emissive phase. The final PL intensities of the OA-QDs and PFDA-QDs films at 4 h are 104% and 354%. Therefore, PFDA modification improves the durability of the QDs.

The PL peak position of the OA-QDs film is shifted from 514.5 to 519.2 nm, similar to the PL redshift of the OA-QDs dispersion. However, the peak position of the PFDA-QDs film shows a redshift from 512.1 to 522.2 nm, while that of its dispersion shows a blueshift. The absence of solvent prevents the preferential dissolution of iodine ions, which results in no change in the Br/I ratio of the QDs in the film. Therefore, the PL redshift is probably observed because of quantum size effects associated with the crystal growth, as observed in the TEM analysis. It should be noted that the influence of the phase transition on the PL peak shift should be negligible because the E_g values for the cubic and monoclinic phases are similar [42].

4. Conclusion

In this work, the influence of PFDA modification on $CsPb(Br,I)_3$ QDs prepared by the LARP method was investigated. Significant aggregation and quenching of green emission under UV light were observed for toluene dispersions of OA-QDs and DA-QDs upon heating at 100°C for 4 h, while the PFDA-QDs dispersion maintained its strong luminescence without precipitation, revealing that PFDA stabilizes the dispersibility and PL of these QDs through surface modification. The rigid adsorption of PFDA also contributed to the suppression of crystal growth, as observed by TEM analysis. Heat treatment was observed to decrease the E_g of OA-QDs and DA-QDs in toluene because of crystal growth upon dissolution and reprecipitation. Conversely, E_g for the PFDA-QDs increased during heating, indicating a decrease of I/Br ratio in the QDs by the preferential dissolution of iodine ions. Improved thermal resistance upon PFDA modification was also observed for the dried QD film. Furthermore, the final PL intensity of the PFDA-QDs film after heating at 80°C for 4 h was 354% of the initial value. These improvements to PL and thermal resistance by PFDA modification have great significance in terms of

the practical application of $CsPb(Br,I)_3$ perovskite QDs to optoelectronic devices that heat up during use, such as LEDs and wide-gamut displays.

Data accessibility. The data are provided in the electronic supplementary material [43].

Authors' contributions. Y.I.: conceptualization, formal analysis, funding acquisition, investigation, methodology, project administration, supervision, writing—original draft; M.E.: formal analysis, investigation, methodology; R.H.: formal analysis, investigation, methodology; K.K.: formal analysis, investigation; T.I.: supervision, writing—review and editing.

All authors gave final approval for publication and agreed to be held accountable for the work performed therein.

Conflict of interest declaration. The authors declare no competing financial interests.

Funding. This work was supported by the JSPS KAKENHI (grant no. JP20K15131) and the Mizuho Foundation for the Promotion of Sciences.

References

1. Kovalenko MV, Protesescu L, Bodnarchuk MI. 2017 Properties and potential optoelectronic applications of lead halide perovskite nanocrystals. *Science* **358**, 745–750. (doi:10.1126/science.aam7093)
2. Iso Y, Isobe T. 2018 Review—synthesis, luminescent properties, and stabilities of cesium lead halide perovskite nanocrystals. *ECS J. Solid State Sci. Technol.* **7**, R3040–R3045. (doi:10.1149/2.0101801jss)
3. Cuan J, Zhang DN, Xing WZ, Han JJ, Zhou H, Zhou Y. 2021 Confining $CsPbX_3$ perovskites in a hierarchically porous MOF as efficient and stable phosphors for white LED. *Chem. Eng. J.* **425**, 131 556–131 562. (doi:10.1016/j.cej.2021.131556)
4. Zhao Y, Xie C, Zhang X, Yang P. 2021 $CsPbX_3$ quantum dots embedded in zeolitic imidazolate framework-8 microparticles for bright white light-emitting devices. *ACS Appl. Nano Mater.* **4**, 5478–5485. (doi:10.1021/acsanm.1c00840)
5. Chen C, Li D, Wu Y, Chen C, Zhu ZG, Shih WY, Shih WH. 2020 Flexible inorganic $CsPbI_3$ perovskite nanocrystal-PMMA composite films with enhanced stability in air and water for white light-emitting diodes. *Nanotechnology* **31**, 225602. (doi:10.1088/1361-6528/ab7648)
6. Cao P, Yang B, Zheng F, Wang L, Zou J. 2020 High stability of silica-wrapped $CsPbBr_3$ perovskite quantum dots for light emitting application. *Ceram. Int.* **46**, 3882–3888. (doi:10.1016/j.ceramint.2019.10.114)
7. Wang H *et al.* 2019 Trifluoroacetate induced small-grained $CsPbBr_3$ perovskite films result in efficient and stable light-emitting devices. *Nat. Commun.* **10**, 665. (doi:10.1038/s41467-019-08425-5)
8. Yao JS *et al.* 2019 Few-nanometer-sized α-$CsPbI_3$ quantum dots enabled by strontium substitution and iodide passivation for efficient red-light emitting diodes. *J. Am. Chem. Soc.* **141**, 2069–2079. (doi:10.1021/jacs.8b11447)
9. Park JH, Lee AY, Yu JC, Nam YS, Choi Y, Park J, Song MH. 2019 Surface ligand engineering for efficient perovskite nanocrystal-based light-emitting diodes. *ACS Appl. Mater. Interfaces* **11**, 8428–8435. (doi:10.1021/acsami.8b20808)
10. Mo Q, Chen C, Cai W, Zhao S, Yan D, Zang Z. 2021 Room temperature synthesis of stable zirconia-coated $CsPbBr_3$ nanocrystals for white light-emitting diodes and visible light communication. *Laser Photonics Rev.* **15**, 2100278. (doi:10.1002/lpor.202100278)
11. Wang B, Kong YC, Chen ZK, Li XS, Wang SP, Zeng QG. 2020 Thermal stability and photoluminescence of Mn^{2+} activated green-emitting feldspar phosphor $SrAl_2Si_2O_8$: Mn^{2+} for wide gamut w-LED backlight. *Opt. Mater.* **99**, 109535. (doi:10.1016/j.optmat.2019.109535)
12. Tong J, Wu J, Shen W, Zhang Y, Liu Y, Zhang T, Nie S, Deng Z. 2019 Direct hot-injection synthesis of lead halide perovskite nanocubes in acrylic monomers for ultrastable and bright nanocrystal–polymer composite films. *ACS Appl. Mater. Interfaces* **11**, 9317–9325. (doi:10.1021/acsami.8b20681)
13. Miyata S, Iso Y, Isobe T. 2019 Green photoluminescence of perovskite $CsPb(Br_{1-x}I_x)_3$ nanocrystals for wide color gamut displays. *ACS Omega* **4**, 15 067–15 073. (doi:10.1021/acsomega.9b01858)
14. Yin Y *et al.* 2020 Full-color micro-LED display with $CsPbBr_3$ perovskite and CdSe quantum dots as color conversion layers. *Adv. Mater. Technol.* **5**, 2000251. (doi:10.1002/admt.202000251)
15. Zhang Q, Su R, Liu X, Xing J, Sum TC, Xiong Q. 2016 High-quality whispering-gallery-mode lasing from cesium lead halide perovskite nanoplatelets. *Adv. Funct. Mater.* **26**, 6238–6245. (doi:10.1002/adfm.201601690)
16. Markina DI *et al.* 2020 Perovskite nanowire lasers on low-refractive-index conductive substrate for high-Q and low-threshold operation. *Nanophotonics* **9**, 3977–3984. (doi:10.1515/nanoph-2020-0207)
17. Li F *et al.* 2021 Single-mode lasing of $CsPbBr_3$ perovskite NWs enabled by the Vernier effect. *Nanoscale* **13**, 4432–4438. (doi:10.1039/D0NR08644D)
18. Wang B, Peng J, Yang X, Cai W, Xiao H, Zhao S, Zang Z. 2022 Template assembled large-size $CsPbBr_3$ nanocomposite films toward flexible, stable, and high-performance X-ray scintillators. *Laser Photonics Rev.* **16**, 2100736. (doi:10.1002/lpor.202100736)
19. Jiang Y, Yuan J, Ni Y, Yang J, Wang Y, Jiu T, Yuan M, Chen J. 2018 Reduced-dimensional α-$CsPbX_3$ perovskites for efficient and stable photovoltaics. *Joule* **2**, 1356–1368. (doi:10.1016/j.joule.2018.05.004)
20. Zhang J, Hodes G, Jin Z, (Frank) Liu S. 2019 All-inorganic $CsPbX_3$ perovskite solar cells: progress and prospects. *Angew. Chem. Int. Ed.* **58**, 15 596–15 618. (doi:10.1002/anie.201901081)
21. Matondo T, Malouangou DM, Bai L, Yang Y, Ondze JN, Bimenyimana T, Guli M. 2021 Recent progress in tailoring the properties of inorganic $CsPbX_3$ perovskites with functional organic compounds: a route to enhanced efficiency and operational stability in $CsPbX_3$-based photovoltaics. *J. Mater. Chem. C* **9**, 9377–9399. (doi:10.1039/D1TC02270A)
22. Zhang W, Liu X, He B, Gong Z, Zhu J, Ding Y, Chen H, Tang Q. 2020 Interface engineering of imidazolium ionic liquids toward efficient and stable $CsPbBr_3$ perovskite solar cells. *ACS Appl. Mater. Interfaces* **12**, 4540–4548. (doi:10.1021/acsami.9b20831)
23. Ullah S *et al.* 2021 Evaporation deposition strategies for all-inorganic $CsPb(I_{1-x}Br_x)_3$ perovskite solar cells: recent advances and perspectives. *Sol. RRL* **5**, 2100172. (doi:10.1002/solr.202100172)
24. Song P, Hase S, Zhao S, Xu Z, Iso Y, Isobe T. 2022 Feasibility of emission-enhanced $CsPbCl_3$ quantum dots co-doped with Mn^{2+} and Er^{3+} as luminescent downshifting layers in crystalline silicon solar modules. *ACS Appl. Nano Mater.* **5**, 2522–2531. (doi:10.1021/acsanm.1c04195)
25. Wei Y, Cheng Z, Lin J. 2019 An overview on enhancing the stability of lead halide perovskite quantum dots and their applications in phosphor-converted LEDs. *Chem. Soc. Rev.* **48**, 310–350. (doi:10.1039/C8CS00740C)
26. Swarnkar A, Mir WJ, Nag A. 2018 Can B-site doping or alloying improve thermal- and phase-stability of all-inorganic $CsPbX_3$ (X=Cl, Br, I) perovskites? *ACS Energy Lett.* **3**, 286–289. (doi:10.1021/acsenergylett.7b01197)
27. Seth S, Ahmed T, De A, Samanta A. 2019 Tackling the defects, stability, and photoluminescence of $CsPbX_3$ perovskite nanocrystals. *ACS Energy Lett.* **4**, 1610–1618. (doi:10.1021/acsenergylett.9b00849)
28. Shen X *et al.* 2019 Enhancing the efficiency of $CsPbX_3$ (X = Cl, Br, I) nanocrystals *via* simultaneous surface peeling and surface passivation. *Nanoscale* **11**, 11 464–11 469. (doi:10.1039/C9NR03679B)
29. Li F, Liu Y, Wang H, Zhan Q, Liu Q, Xia Z. 2018 Postsynthetic surface trap removal of

$CsPbX_3$ (X = Cl, Br, or I) quantum dots via a ZnX_2 hexane solution toward an enhanced luminescence quantum yield. *Chem. Mater.* **30**, 8546–8554. (doi:10.1021/acs.chemmater.8b03442)

30. Jia C, Li H, Meng X, Li H. 2018 $CsPbX_3/Cs_4PbX_6$ core/shell perovskite nanocrystals. *Chem. Commun.* **54**, 6300–6303. (doi:10.1039/C8CC02802H)
31. Zhang F *et al.* 2019 Synergetic effect of the surfactant and silica coating on the enhanced emission and stability of perovskite quantum dots for anticounterfeiting. *ACS Appl. Mater. Interfaces* **11**, 28 013–28 022. (doi:10.1021/acsami.9b07518)
32. Kidokoro K, Iso Y, Isobe T. 2019 Complete self-recovery of photoluminescence of photodegraded cesium lead bromide quantum dots. *J. Mater. Chem. C* **7**, 8546–8550. (doi:10.1039/C9TC02365H)
33. Miyashita K, Kidokoro K, Iso Y, Isobe T. 2021 Effects of halide composition on the self-recovery of photodegraded cesium lead halide perovskite nanocrystals: implications for photoluminescence applications. *ACS Appl. Nano Mater.* **4**, 12 600–12 608. (doi:10.1021/acsanm.1c03119)
34. Sato D, Iso Y, Isobe T. 2020 Effective stabilization of perovskite cesium lead bromide nanocrystals through facile surface modification by perfluorocarbon acid. *ACS Omega* **5**, 1178–1187. (doi:10.1021/acsomega.9b03472)
35. Moroi Y, Yano H, Shibata O, Yonemitsu T. 2001 Determination of acidity constants of perfluoroalkanoic acids. *Bull. Chem. Soc. Jpn* **74**, 667–672. (doi:10.1246/bcsj.74.667)
36. Salentinig S, Sagalowicz L, Glatter O. 2010 Self-assembled structures and pK_a value of oleic acid in systems of biological relevance. *Langmuir* **26**, 11 670–11 679. (doi:10.1021/la101012a)
37. Miyata S, Iso Y, Isobe T. 2021 Investigation on photoluminescence of $CsPb(Br,I)_3$ perovskite nanocrystals by comparison between hot-injection and ion-exchange methods. *ECS J. Solid State Sci. Technol.* **10**, 096003. (doi:10.1149/2162-8777/ac202a)
38. Tauc J, Menth A. 1972 States in the gap. *J. Non-Cryst. Solids* **8–10**, 569–585. (doi:10.1016/0022-3093(72)90194-9)
39. Protesescu L, Yakunin S, Bodnarchuk MI, Krieg F, Caputo R, Hendon CH, Yang RX, Walsh A, Kovalenko MV. 2015 Nanocrystals of cesium lead halide perovskites ($CsPbX_3$, X = Cl, Br, and I): novel optoelectronic materials showing bright emission with wide color gamut. *Nano Lett.* **15**, 3692–3696. (doi:10.1021/nl5048779)
40. Enomoto I, Iso Y, Isobe T. 2022 Implications of gas-barrier properties in realizing the self-recovery of photodegraded $CsPbBr_3$ perovskite nanocrystals. *J. Mater. Chem. C* **10**, 102–107. (doi:10.1039/D1TC05077J)
41. Gan Z, Wen X, Chen W, Zhou C, Yang S, Cao G, Ghiggino KP, Zhang H, Jia B. 2019 The dominant energy transport pathway in halide perovskites: photon recycling or carrier diffusion? *Adv. Energy Mater.* **9**, 1900185. (doi:10.1002/aenm.201900185)
42. Wang S *et al.* 2020 Mesoporous-carbon-based fully-printable all-inorganic monoclinic $CsPbBr_3$ perovskite solar cells with ultrastability under high temperature and high humidity. *J. Phys. Chem. Lett.* **11**, 9689–9695. (doi:10.1021/acs.jpclett.0c02739)
43. Iso Y, Eri M, Hiroyoshi R, Kano K, Isobe T. 2022 Improving the thermal resistance of fluorescent $CsPb(Br,I)_3$ perovskite quantum dots by surface modification with perfluorodecanoic acid. Figshare. (doi:10.6084/m9.figshare.c.6135601)